

Cite this article as: Yu Zhiqi, Zhao Yanchun, Liu Tianzeng, et al. Effect of Cu and Mo Alloying on Microstructure and Molten Salt Corrosion Resistance of 347H Stainless Steel[J]. Rare Metal Materials and Engineering, 2025, 54(04): 862-870. DOI: <https://doi.org/10.12442/j.issn.1002-185X.20240122>.

ARTICLE

Effect of Cu and Mo Alloying on Microstructure and Molten Salt Corrosion Resistance of 347H Stainless Steel

Yu Zhiqi¹, Zhao Yanchun¹, Liu Tianzeng^{1,2}, Feng Li¹, Ma Huwen¹, Li Jucang², Pan Jixiang²

¹ State Key Laboratory of Advanced Processing and Recycling of Nonferrous Metals, School of Materials Science and Engineering, Lanzhou University of Technology, Lanzhou 730050, China; ² Gansu Jiu Steel Group Hongxing Iron & Steel Co., Ltd, Jiayuguan 735100, China

Abstract: A static corrosion experiment of 347H stainless steel alloyed with elements Cu and Mo was carried out in a nitrate molten salt (60% NaNO₃+40% KNO₃) at 565 °C for 720 h. The effects of elements Cu and Mo on the corrosion resistance of 347H stainless steel in molten salt were investigated by analyzing the phase composition, microstructure and chemical composition of the corrosion products. The results show that the grain refinement induced by element Mo imparts the stainless steel with optimal corrosion resistance at a medium grain size. Furthermore, the formation of MoC significantly enhances the intergranular corrosion resistance of the stainless steel. The stainless steel exhibits uniform corrosion in the nitrate solution. The corrosion layer displays a dual-layer structure, and the corrosion products protecting matrix are present in both the inner and outer layers. The outer layer consists of a mixture of Fe oxides (Fe₂O₃, Fe₃O₄), NaFeO₂, and a minor amount of MgFe₂O₄. Conversely, the inner layer is primarily composed of a spinel layer (FeCr₂O₄, MgCr₂O₄) and a thin Cu₂O layer. The oxidation of Cu in the inner layer leads to the formation of a dense Cu₂O layer, effectively impeding O²⁻ plasma infiltration into the matrix.

Key words: alloying; 347H stainless steel; nitrate; molten salt corrosion

1 Introduction

Concentrated solar power (CSP) technology, recognized for its maturity, cost-effective energy storage, and controllable output power, has become a crucial approach for large-scale solar power generation^[1-2]. The high adjustability and conversion efficiency of this technology relies on reliable high-temperature heat storage and molten salt heat transfer performance. Currently, the predominant salt mixture utilized in CSP plants is a nitrate consisting of 60% NaNO₃ and 40% KNO₃, which demonstrates stable thermal behavior below 600 °C^[3-5]. However, the application of high-temperature nitrate molten salts normally results in corrosion of storage tanks and pipelines, a phenomenon significantly influenced by impurity levels and the alloy composition in the salt. Impurities play a critical role in the corrosion of materials^[6-7]. Commercial nitrates, typically of analytical purity, often contain impurities such as chlorides, nitrites, and H₂O^[8].

Among these, Cl⁻ ions can disrupt surface oxide films, compromising their protective function. At high temperature, some nitrates decompose into nitrites and O², where O² reacts with elemental components, and H₂O accelerates the cathodic corrosion reaction, exacerbating corrosion^[9-11]. The composition of alloys directly impacts the chemical composition and structure of surface oxide films, consequently influencing the corrosion resistance of the material^[12]. Studies indicate that carbon steel forms a dual-layer structured oxide film on the surface after corrosion in nitrates, with an inner layer of Fe₃O₄ that further oxidizes to form an outer layer of Fe₂O₃^[13]. On the contrary, stainless steel forms an oxide film consisting of FeCr₂O₄, Fe₃O₄, and NaFeO₂, sequentially from the substrate to the surface^[14]. The protective efficacy of oxide films on the substrate is primarily determined by the properties of the oxides, i. e., dense and tightly bound oxides offer superior protection, while porous structures are less effective^[15].

Received date: April 06, 2024

Foundation item: Science and Technology Program Project of Gansu Province (21ZD3GB001)

Corresponding author: Zhao Yanchun, Ph. D., Professor, State Key Laboratory of Advanced Processing and Recycling of Nonferrous Metals, School of Materials Science and Engineering, Lanzhou University of Technology, Lanzhou 730050, P. R. China, E-mail: zhaoyanchun@edu.lut.cn

Copyright © 2025, Northwest Institute for Nonferrous Metal Research. Published by Science Press. All rights reserved.

Stainless steel has emerged as the primary choice for molten salt storage tanks in CSP plants owing to its exceptional corrosion resistance and high-temperature capabilities^[16]. The 347H stainless steel, a chromium-nickel-niobium austenitic variant, benefits from niobium's role in stabilizing carbon atoms, which prevents the precipitation of Cr₂₃C₆ at grain boundaries^[17]. This characteristic imparts outstanding resistance to intergranular corrosion and ensures strong structural stability. Alloying, the process of introducing one or more elements under specific conditions to produce an alloy with desired properties, can further enhance the corrosion resistance of stainless steel^[18-19]. Nevertheless, research on the corrosion resistance of 347H stainless steel after alloying treatments in molten salt environments is few. Consequently, this study investigated the effect of Cu and Mo alloying on 347H austenitic stainless steel and evaluated their effects on corrosion behavior within a binary mixed nitrate melt (60% NaNO₃+40% KNO₃) at 565 °C for up to 720 h. The insights gained from this research endeavor aim to offer theoretical backing for enhancing the corrosion resistance of heat transfer and thermal storage apparatus in CSP systems.

2 Experiment

In this study, 8 mm thick plates of J347H austenitic stainless steel were prepared through an alloying process involving the addition of elements Cu and Mo. The plates were hot rolled at 1165 °C for 30 min, followed by water quenching. Subsequently, samples with dimension of 25 mm×25 mm×10 mm were cut using wire cutting, polished, and cleaned to determine the surface area. The samples were then weighed using an electronic balance and sealed for further analysis. Analytically pure NaNO₃ and KNO₃ salts were weighed and mixed in a 6:4 mass ratio. Impurities present in the salts are listed in Table 1. The mixture was then heated at 300 °C in a muffle furnace for 48 h to eliminate moisture from the salts.

A sufficient quantity of the mixed salt was added into crucibles to ensure complete immersion of the samples, which were then placed in the muffle furnace for static immersion corrosion testing at 565 °C for 120, 240, 360, 480, 600, and 720 h. The atmosphere in contact with the molten salt was air, and no artificial gases were introduced into the furnace chamber. After the corrosion testing, the crucibles were removed for cooling, and the samples were cleaned with deionized water and anhydrous ethanol, dried, and weighed

Table 1 Impurity content in two nitrates (%)

Nitrate	NO ₂ ⁻	Cl ⁻	Mg ²⁺	SO ₄ ²⁻	Ca ²⁺
NaNO ₃	≤0.0005	≤0.0015	≤0.001	≤0.003	≤0.005
KNO ₃	≤0.001	≤0.003	≤0.002	≤0.003	≤0.004

Table 2 Chemical composition of J347H alloys (wt%)

C	Si	Mn	P	S	Cr	Ni	Nb	N	Cu	Mo	Fe
0.06	0.53	1.13	0.025	0.0006	17.45	9.14	0.56	0.013	0.39	0.45	Bal.

using a high-precision electronic balance. The mass gain per unit area, Δm_s (g/cm²), was calculated by Eq.(1).

$$\Delta m_s = \frac{m_i - m_f}{A_0} \quad (1)$$

where m_i is the post-corrosion mass, m_f is the pre-corrosion mass, and A_0 is the surface area.

The annual corrosion rate R (mm/a) was calculated using Eq.(2).

$$R = 8760 \frac{m_0 - m_1}{S_0 t \rho} \quad (2)$$

where m_0 is the pre-corrosion mass, m_1 is the post-corrosion mass, S_0 is the pre-corrosion area, t is the corrosion time, and ρ is the sample density.

The actual chemical composition of J347H stainless steel was tested by Magix-Pw2403 fluorescence emission spectrometer, and the results are shown in Table 2. The microstructure was observed with an inverted metallographic microscope (OM, LSXTL18A). Thin sections of the samples were examined using a FEI-TECNAI G2 transmission electron microscope (TEM) for microstructure and second phase observation. The surface phases of the samples and corrosion products were analyzed using a Bruker D8 Advance X-ray diffractometer (XRD) with Cu K α radiation at a scanning speed of 4°/min. The morphology, structure, and chemical composition of the corrosion layer were investigated with a Gemini 300 field emission scanning electron microscope (SEM) equipped with an energy dispersive spectrometer (EDS). The elemental chemical state of surface and distribution of the corrosion layer were characterized using an ASIX SUPRA⁺ X-ray photoelectron spectrometer (XPS).

3 Results and Discussion

3.1 Microstructure analysis

The microstructure of J347H stainless steel is shown in Fig. 1a, where the stainless steel matrix is austenite with equiaxed grains, and its grain boundaries are relatively flat. XRD phase analysis of the J347H stainless steel surface is illustrated in Fig. 1b. The analysis reveals a predominance of austenitic phases on the stainless steel surface, accompanied by a minor fraction of ferritic phases. The high chromium content in 347H steel promotes the formation of ferritic phases since chromium acts as a ferrite stabilizer, while the low carbon content in the austenite facilitates ferrite formation. This phenomenon is discernible in the diffraction patterns that exhibit peaks corresponding to ferrite. For rolled J347H, the austenitic phase demonstrates a preferred orientation along (111), with discernible peaks indicating the presence of ferritic phases at diffraction angles of 44° and 82°.

Fig.2 is TEM and SAED analysis results of the matrix and precipitated phase of J347H stainless steel. As shown in

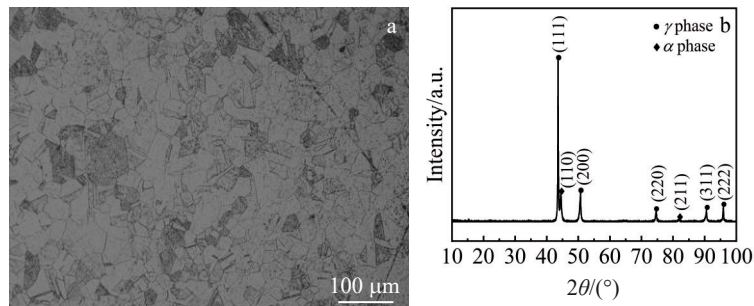


Fig.1 Metallographic micrograph (a) and XRD pattern (b) of J347H stainless steel

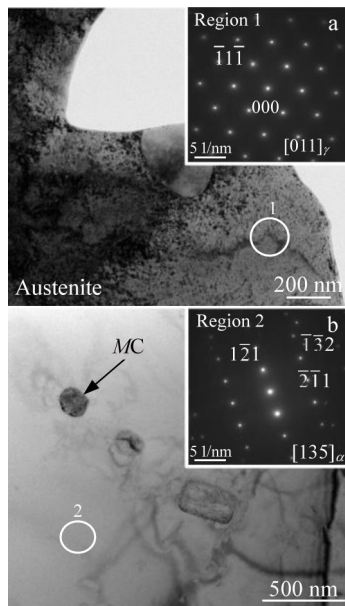


Fig. 2 TEM images and SAED patterns of J347H stainless steel: (a) austenitic phase and (b) carbide

Fig.2a and 2b, the matrix of J347H stainless steel consists of austenite phases with a minor presence of ferrite phases. In addition, there are precipitated phases in the matrix, as shown in Fig. 2b. These precipitates are analyzed as MC-type carbides, which are distributed in the grain, avoiding the risk of intergranular corrosion caused by carbide precipitation at grain boundaries.

Fig.3a reveals that the average grain size of J347H stainless steel is $49.3 \mu\text{m}$, corresponding to a grade 7 average grain size, with minor occurrences of annealing twin. SEM image in Fig. 3b shows that the granular carbides (white) in J347H stainless steel are dispersedly distributed in the crystal. Compared with the hot-rolled 347H stainless steel, the carbides are smaller in size and fewer in number. This phenomenon occurs because solid solution treatment causes the carbides to dissolve into the austenite matrix at high temperature, followed by the reprecipitation of a small quantity of carbides with fine particles and even distribution. Fig.3c illustrates the MC carbides and EDS results, revealing predominantly NbC and MoC. When the high chromium carbide (Cr_{23}O_6) precipitates along the intergranular, the local

chromium depletion around the carbide will cause intergranular corrosion. Like element Nb, the binding ability of element Mo and element C is much stronger than that of element Cr, so C is completely combined with Mo and Nb, thus effectively preventing Cr and C from combining to precipitate Cr_{23}O_6 . It can be seen from the cross-section morphology of J347H after 720 h corrosion that the surface of the substrate near the corrosion layer of J347H stainless steel is smoother than that of conventional 347H. Table 3 suggests that NbC constitutes approximately 75%, while MoC accounts for around 25%, indicating a substantial allocation of Mo to the matrix during solidification, contributing to grain refinement^[20-21]. Consequently, J347H demonstrates a moderate grain size due to these microstructural characteristics.

3.2 Corrosion kinetics analysis

Using Eq.(1)^[22], the mass gain per unit area of samples after different corrosion duration was calculated, and the corrosion kinetics curve are obtained for J347H stainless steel and conventional 347H stainless steel in a nitrate melt (60% NaNO_3 +40% KNO_3) at $565 \text{ }^\circ\text{C}$, as depicted in Fig.4. It can be observed that with increasing the corrosion duration, the corrosion kinetics curve generally follows a parabolic pattern, indicating that the rate of mass gain per unit area slows down over time. In contrast, the corrosion rate of J347H stainless steel is smaller, which means that its corrosion resistance is also better. At the initial stage of corrosion, the sample directly reacts with the molten salt. Corrosion products continuously nucleate, grow, and adhere to the surface of the sample, leading to rapid mass gain. When the corrosion time reaches 360 h, the corrosion kinetics curve begins to plateau. At this time, a relatively complete and stable oxide film is formed on the substrate surface and binds well with the substrate, preventing direct contact between the substrate and the molten salt. Additionally, it slows down the further diffusion of impurity atoms from the molten salt into the stainless steel substrate, thereby reducing the mass gain rate in the later stages of corrosion. Further analysis of the corrosion layer structure reveals that the element Cu added to J347H forms a dense Cu_2O thin layer on the stainless steel surface. Even with the presence of Cl⁻ impurities in the molten salt, it provides protective effects to the substrate^[23-24]. The element Mo in J347H stainless steel acts as a solid solution element that strengthens the atomic bonds within the solid solution,

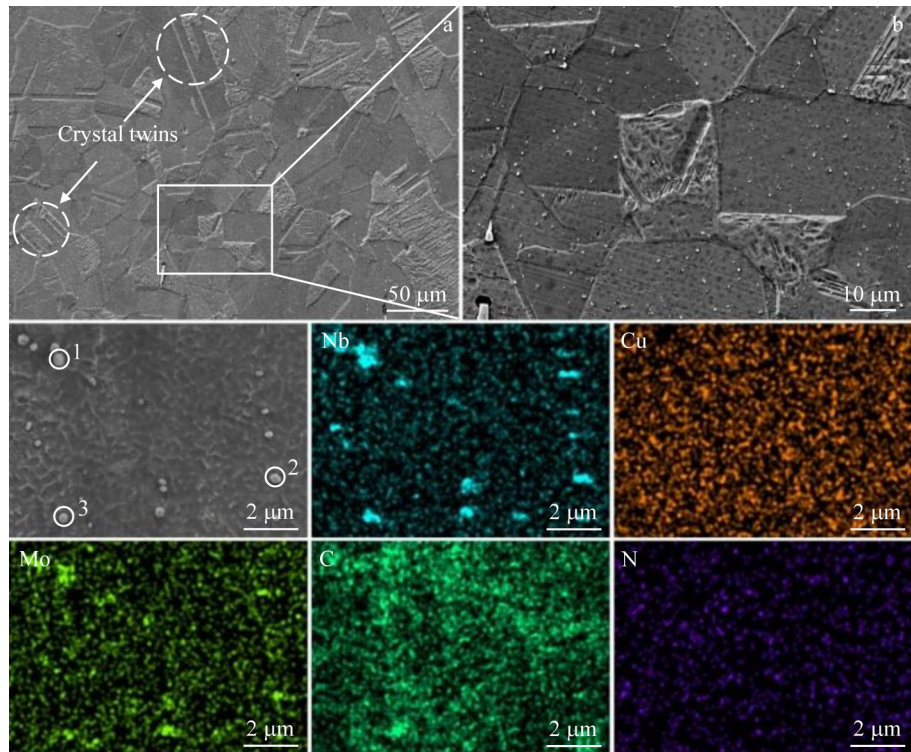


Fig.3 SEM images of J347H stainless steel (a–b); microstructure of *MC* carbides and corresponding EDS results (c)

Table 3 EDS results of second phases marked in Fig.3c (at%)

Point	Nb	Cu	Mo	C	N
1	40.78	0.04	10.09	48.50	0.58
2	41.03	0.17	7.94	50.13	0.73
3	36.06	0.21	10.90	52.37	0.46

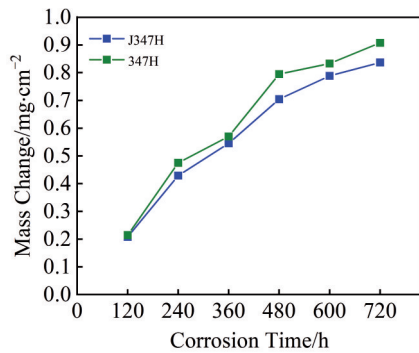


Fig.4 Corrosion kinetic curve of stainless steels in binary mixed nitric acid molten salt at 565 °C

reducing the high-temperature diffusion rate of atoms and thus slowing down the oxidation rate of the stainless steel^[24]. Utilizing Eq. (2)^[25], the mass gain after 720 h of corrosion yields an annual corrosion rate of only 0.0096 mm/a for J347H stainless steel in a binary mixture of nitrate melt at 565 °C. Tang et al^[26] calculated the annual corrosion rate for 347H stainless steel subjected to a solution treatment at 1160 °C for 1 h, which is 0.0132 mm/a. This comparison demonstrates that the J347H stainless steel, containing

elements Cu and Mo, exhibits superior resistance to high-temperature molten salt corrosion than conventional 347H stainless steel.

3.3 Analysis of corrosion products

Fig. 5 presents XRD analysis results of the corrosion products on the surface of J347H stainless steel after exposure to a binary mixture of nitrate melt (60% NaNO₃+40% KNO₃) at 565 °C for various durations: 120, 240, 360, 480, 600, and 720 h. The corrosion products consist of oxides (Fe₂O₃ and Fe₃O₄) and spinel structures (MgCr₂O₄, MgFe₂O₄ and FeCr₂O₄), along with NaFeO₂. Initially, the quantity of corrosion products is minimal, and the surface is primarily composed of austenite phase. As the corrosion duration extends, the intensity of the diffraction peaks corresponding to the corrosion products intensifies, indicating an increased content of corrosion products. After 600 h of corrosion, no significant changes in the peak intensities of various corrosion products are observed, suggesting the formation of a stable structure on the stainless steel surface.

At elevated temperatures, partial decomposition of NO₃⁻ in nitrate salts generates NO₂⁻ and O²⁻ (Eq.(3)), which is one of the primary sources for the corrosive nature of the molten salts^[11].



The primary corrosion product of stainless steel immersed in nitric acid molten salt is Fe₃O₄, formed via two pathways: direct redox reaction between Fe and nitrate ions (NO₃⁻) in the matrix (Eq.(4)), and anodic oxidation of Fe atoms (Eq.(5–6)). Furthermore, Fe interacts with NO₄⁻ ions to generate Fe₂O₃ (Eq.

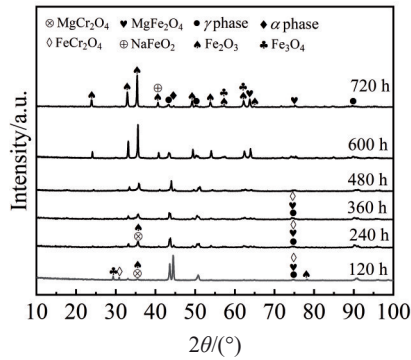
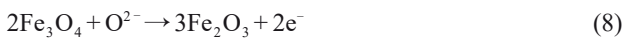
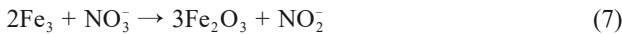
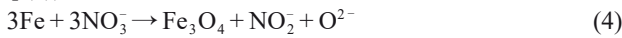


Fig. 5 XRD patterns of surface corrosion products of J347H after different corrosion durations

(7)), while Fe_3O_4 undergoes further oxidation to form Fe_2O_3 (Eq.(8))^[27].



After corrosion for 120 h, the element Cr on the surface of the stainless steel substrate undergoes an oxidation reaction with the O^{2-} generated from the decomposition of NO_3^- in the molten salt to form Cr_2O_3 (Eq. (9)). Subsequently, it reacts with iron oxides to produce the iron chromium spinel, FeCr_2O_4 (Eq.(10)). Meanwhile, Na^+ from the molten salt diffuses to the

outer surface of the oxide layer, forming NaFeO_2 , as shown in Eq. (11) and Eq. (12)^[10,27]. After 240 h of corrosion, trace amount of Mg^{2+} from impurities in the molten salt penetrate the Fe_2O_3 layer to form MgFe_2O_4 (Eq. (13)). Simultaneously, Mg^{2+} and O^{2-} diffuse into the inner layers and react with Cr_2O_3 to form the spinel structure of MgCr_2O_4 (Eq.(14))^[5].

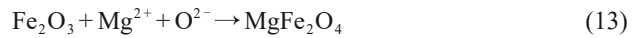


Fig.6a–6f depict the morphologies of corrosion products on the surface of J347H stainless steel at various corrosion durations. When the corrosion reaches 120 h, scattered granular corrosion products appear on the surface of the sample. After 240 h, fine plate-like corrosion products appear, which fully transform into granular form at 600 h, and after 720 h, they completely cover the substrate surface. Throughout the corrosion process, as the duration increases, the granular corrosion products increase in size, reaching 2–5 μm after 720 h. The corrosion layer adheres well to the substrate, and no significant delamination of the corrosion layer is observed^[28]. Fig.6g illustrates EDS analysis results of the surface of J347H stainless steel after 720 h of corrosion. It is apparent that the outer layer of the corrosion product is predominantly composed of an iron oxide layer and sodium

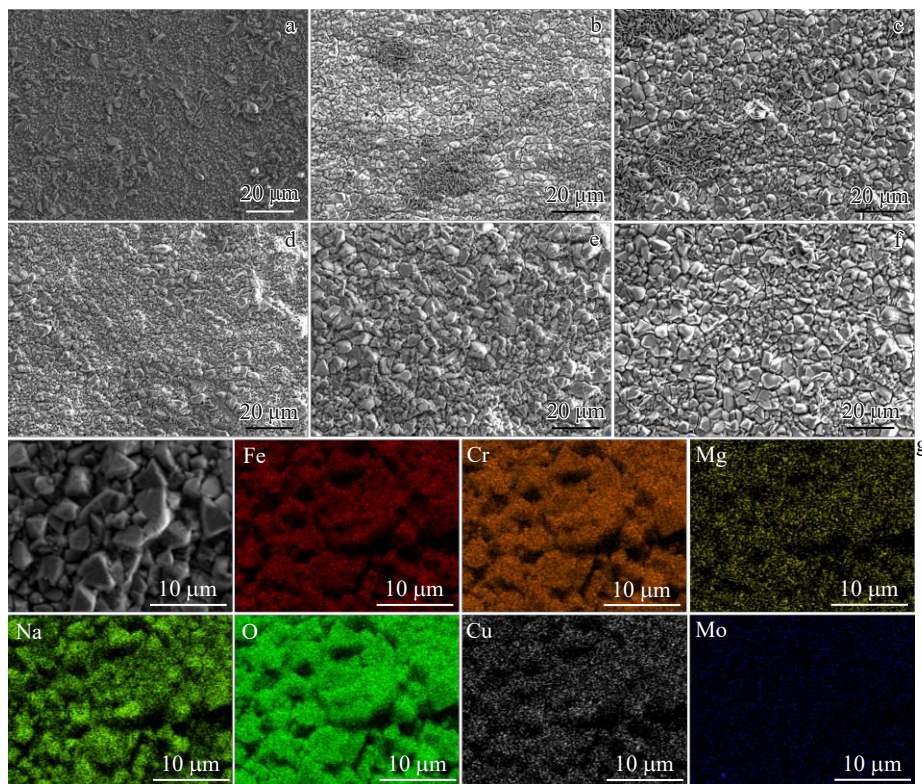


Fig.6 Morphologies (a–f) and EDS analysis (g) of corrosion products of J347H after different corrosion durations: (a) 120 h, (b) 240 h, (c) 360 h, (d) 480 h, (e) 600 h, and (f–g) 720 h

Table 4 EDS results of J347H corrosion products (wt%)

Corrosion time/h	Fe	O	Na	Mg	Cr
120	50.82	40.66	5.6	-	2.04
720	50.05	35.99	11.19	1.50	-

ferrite particles (NaFeO_2). According to Table 4, at 120 h, the surface of the corrosion layer consists mainly of elements Fe and O, with minor quantity of Na and Cr. In conjunction with XRD analysis, the corrosion products at this stage are identified as Fe_2O_3 , Fe_3O_4 , FeCr_2O_4 and NaFeO_2 . At 720 h, the Na content on the surface of the corrosion layer increases, and element Mg is detected, while element Cr is not observed. XRD analysis indicates that the corrosion layer at this point consists primarily of iron oxides (Fe_2O_3 and Fe_3O_4), NaFeO_2 , and a minor quantity of MgFe_2O_4 .

Fig. 7a illustrates XPS survey spectrum of the corrosion layer on J347H stainless steel, indicating that the outer layer is predominantly composed of iron oxides. Deconvolution of the peaks for each element provides detailed spectra. Fig. 7b depicts the Fe 2p spectrum. Iron is identified in the forms of FeOOH , Fe_3O_4 and Fe_2O_3 . Fe_2O_3 exhibits a higher peak intensity than Fe_3O_4 , implying a higher proportion of Fe_2O_3 in the corrosion layer. Fig. 7c showcases the O 1s spectrum, revealing the presence of oxygen in both OH^- and O^{2-} states. OH^- corresponds to hydroxides, while O^{2-} corresponds to oxides. Additionally, Fig. 7d displays the Na 1s spectrum, demonstrating that sodium is exclusively present as Na^+ . Integrating these data with XRD results, it can be suggested that NaFeO_2 is formed.

Fig. 8 illustrates the cross-sectional morphology and elemental analysis of the corrosion layer on J347H stainless steel after 720 h of corrosion. The average thickness of the corrosion layer measures approximately 4 μm , and the interface between the corrosion layer and the metallic substrate appears mostly flat, indicating uniform corrosion. Studies have revealed that corrosion typically initiates at defect sites, such as impurities and inclusions. Significantly, the presence of copper in J347H stainless steel can help alleviate localized corrosion induced by sulfur-containing inclusions^[29]. The corrosion layer of J347H stainless steel displays a double oxide layer structure, consistent with the findings of Kityk et al^[30]. Elements Fe and Mg are distributed throughout both the inner and outer layers, and element Fe is predominant in the outer layer, suggesting that the concentration of iron oxides in the outer layer surpasses that in the inner iron spinel. Magnesium ions within the iron oxide layer contribute to the formation of MgFe_2O_4 . Simultaneously, magnesium ions diffuse into the inner layer to produce MgCr_2O_4 spinel, while sodium ions are accumulated at the outer layer of Fe_2O_3 to produce sodium ferrite (NaFeO_2). Chromium from the substrate diffuses into the corrosion layer and becomes enriched therein, and its concentration decreases from the inside region outward, implying that the chromium spinel is primarily located in the inner layer. Additionally, there is a distinct enrichment of element Cu at the interface between the inner layer and the substrate, resulting in the formation of Cu_2O layer. Furthermore, a narrow region enriched with nickel is observed near the substrate within the inner layer of the corrosion scale, stemming from the

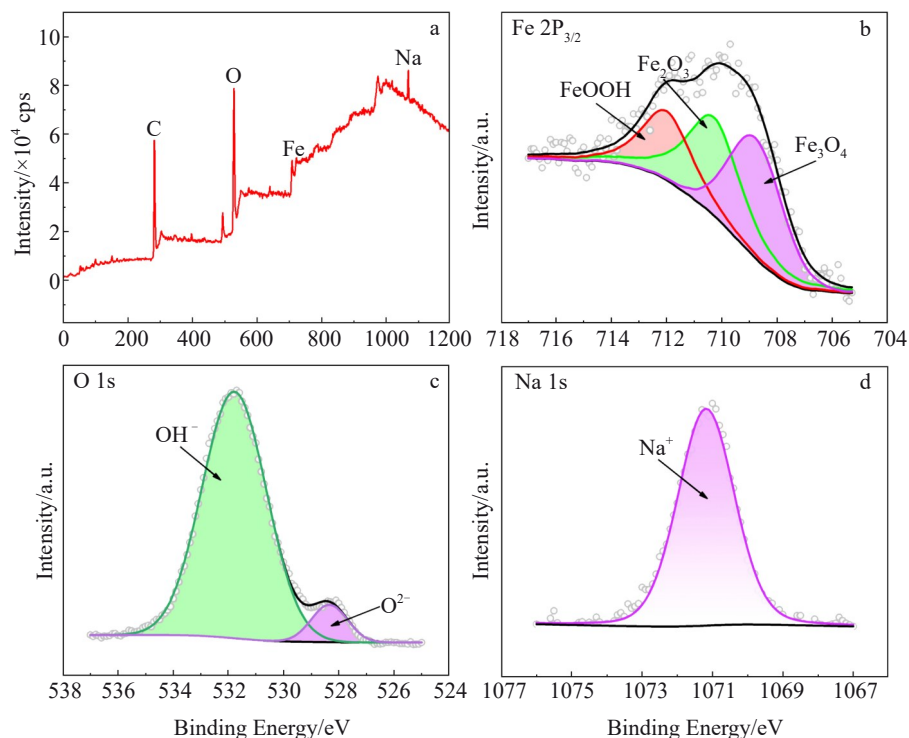


Fig.7 XPS spectra of J347H stainless steel corrosion layer: (a) total map, (b) Fe 2p_{3/2}, (c) O 1s, and (d) Na 1s

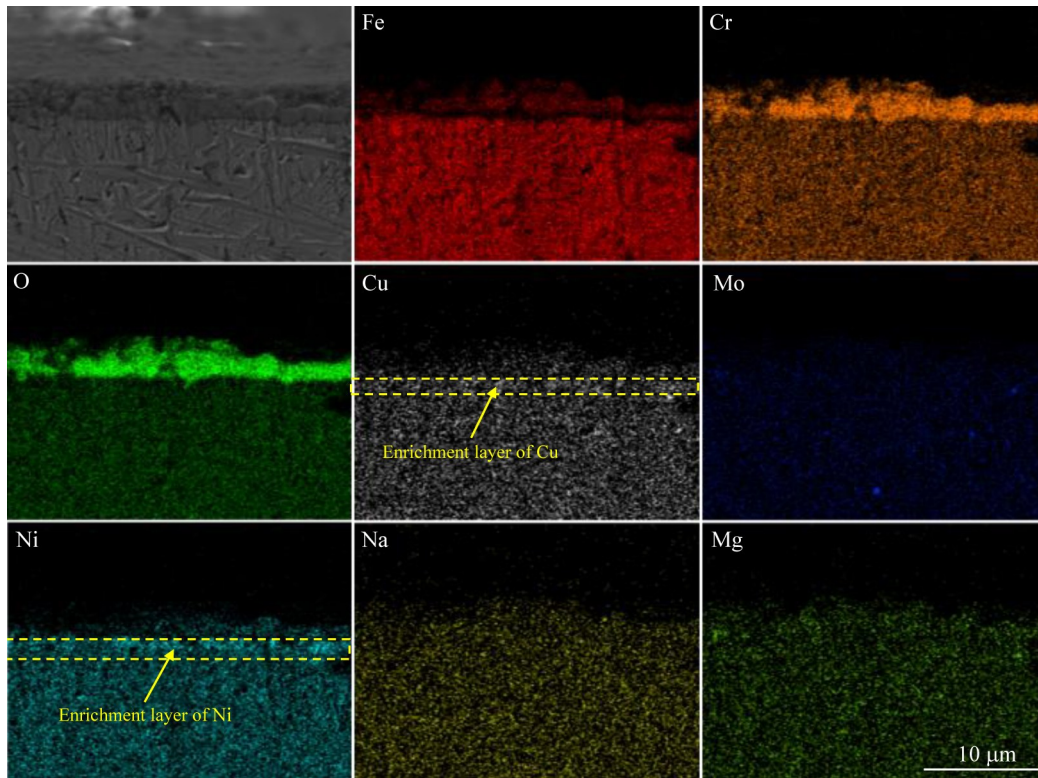


Fig.8 Cross-section corrosion morphology and EDS mappings of J347H stainless steel

depletion of elements Fe and Cr as they diffuse to form the corrosion layer^[22-23,31].

The surface and cross-section morphologies of conventional 347H stainless steel are shown in Fig.9a. The nucleation and growth of the corrosion layer in traditional 347H stainless steel are not uniform, and the corrosion layer is not completely covered. As shown in Fig.6a–6f, the corrosion layer of J347H stainless steel containing Cu is relatively uniform and smooth. Comparing the cross-section morphologies of stainless steel shown in Fig.8 and Fig.9b, it can be seen that the substrate surface of J347H stainless steel containing element Cu is smoother than that of conventional 347H, and no obvious local corrosion phenomenon can be seen.

Fig.10 depicts the schematic structure of the corrosion layer on J347H stainless steel, which consists of an outer layer of iron oxides and sodium ferrite (NaFeO_2), and an inner layer of

(Fe, Cr) spinel and Cu_2O . The porous and loosely packed Fe_2O_3 structure in the corrosion layer exhibits poor corrosion resistance, whereas Fe_3O_4 forms a dense layer strongly adherent to the underlying matrix, providing effective protection against further degradation. According to findings of Fernández et al^[32], a highly crystalline and dense NaFeO_2 layer can protect the inner oxide layer from direct contact with the molten salt, thereby preventing additional corrosion. The inner layer is characterized by FeCr_2O_4 , which exhibits a relative dense structure and strong adhesion to the substrate surface, allowing for the outward diffusion of Fe and the inward transport of O^{2-} ^[32-33]. The formation of MgCr_2O_4 reduces chromium activity, thereby minimizing diffusion and loss of chromium^[34]. Additionally, the compact Cu_2O layer hinders the further reaction of O^{2-} from the molten salt with the substrate elements. The presence of protective corrosion products, both internally and externally, on J347H stainless

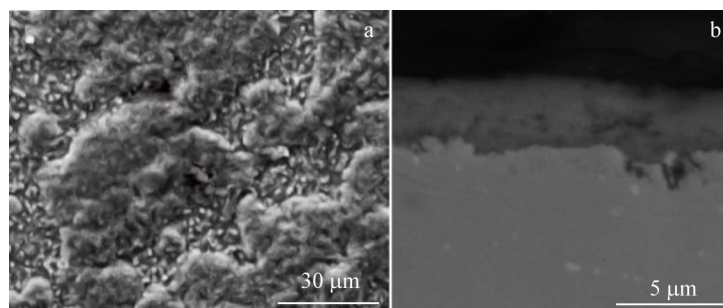


Fig.9 SEM morphologies of surface (a) and cross-section (b) of conventional 347H stainless steel after corrosion for 720 h

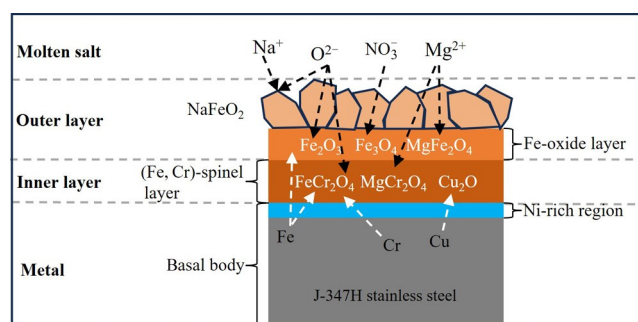


Fig.10 Schematic structure of corrosion layer on J347H stainless steel

steel contributes to its superior corrosion resistance properties.

4 Conclusions

1) The addition of element Mo contributes to grain refinement, resulting in J347H stainless steel exhibiting a medium grain size and, consequently, excellent corrosion resistance. The corrosion kinetics curve of J347H conforms to the parabolic law, and the annual corrosion rate is only 0.0096 mm/a.

2) The corrosion behavior of J347H stainless steel in nitric acid exhibits uniform corrosion, characterized by a dual-layer corrosion product structure. The inner layer consists primarily of spinel phases (FeCr_2O_4 and MgCr_2O_4) and a thin Cu_2O layer, while the outer layer is composed of iron oxides (Fe_2O_3 and Fe_3O_4), NaFeO_2 , and trace amounts of MgFe_2O_4 .

3) The density and stability of corrosion layer products determine whether they provide protective effects on the substrate. In J347H stainless steel, both inner and outer layers of the corrosion layer contain products that can protect the substrate. Specifically, the formation of dense Cu_2O in the inner layer effectively blocks impurity ions like O^{2-} from further reacting with the substrate, imparting excellent corrosion resistance to J347H.

References

- Allan R Starke, José M Cardemil, Vinicius R B Bonini et al. *Applied Energy*[J], 2024, 359: 122689
- Papaalias M, Cheng L, Kogia M et al. *Renewable Energy*[J], 2016, 85: 1178
- Roeb M, Neises M, Monnerie N et al. *Energy & Environmental Science*[J], 2011, 4: 2503
- Vignarooban K, Xu X H, Arvay A et al. *Applied Energy*[J], 2015, 146: 383
- Lopez J, Acem Z, Barrio E P D. *Applied Thermal Engineering*[J], 2010, 30(13):1586
- Ma Lina, Zhang Cancan, Wu Yuting et al. *Solar Energy Materials and Solar Cells*[J], 2022, 235: 111485
- Miguel M T, Lasanta M I, García-Martín G et al. *Corrosion Science*[J], 2022, 201: 110271
- Spiegel M, Schraven P. *Oxidation of Metals*[J], 2021, 96(1–2): 1
- Kruizenga A, Gill D. *Energy Procedia*[J], 2014, 49: 878
- Goods S H, Bradshaw R W. *Journal of Materials Engineering and Performance*[J], 2004, 13(1): 78
- Fernández A G, Galleguillos H, Pérez F J. *Oxidation of Metals*[J], 2014, 82(5–6): 331
- Yang S F, Che Z C, Liu W et al. *Corrosion Science*[J], 2023, 225: 111610
- Fernández A G, Galleguillos H, Pérez F J. *Solar Energy*[J], 2014, 109: 125
- Wang T, Viswanathan S, Mantha D et al. *Solar Energy Materials and Solar Cells*[J], 2012, 102: 201
- Heinzel A, Weisenburger A, Müller G et al. *Materials and Corrosion*[J], 2017, 68(8): 831
- Bauer T, Pflieger N, Breidenbach N et al. *Applied Energy*[J], 2013, 111: 1114
- Chen H, Kim S H, Kim C et al. *Corrosion Science*[J], 2019, 156: 16
- Xu Shitong, Bai Yong, Yao Meiyi et al. *Rare Metal Materials and Engineering*[J], 2023, 52(6): 2169 (in Chinese)
- Niu Jiacheng, Hou Guoliang, Fu Zhiqiang. *Materials China*[J], 2025, 44(1): 84 (in Chinese)
- Lyu Y, Sun Y, Liu S et al. *International Journal Cast Metals Research*[J], 2015, 28(5): 263
- Xu Yongxiang, Zhu Mengzhen, Fang Huachan et al. *Rare Metal Materials and Engineering*[J], 2023, 52(10): 3556 (in Chinese)
- Alexander B, Wenjin D, Andrea H et al. *Corrosion Science*[J], 2024, 227: 111700
- Dorcheh A S, Durham R N, Galetz M C et al. *Solar Energy Materials and Solar Cells*[J], 2016, 144: 109
- Tao X U, Limin C, Jianhua L. *Rare Metals*[J], 2006, 25(3): 210
- Zhou Zuolang, Min Xiaohua, Bai Pengfei et al. *Rare Metal Materials and Engineering*[J], 2023, 52(1): 186 (in Chinese)
- Tang Menglan, Wang Jun, Liu Tianzeng et al. *Journal of Lanzhou University of Technology*[J], 2021, 47(5): 9 (in Chinese)
- Dorcheh A S, Durham R N, Galetz M C. *Materials and Corrosion*[J], 2017, 68: 943
- Agüero A, Audigie P, Rodríguez S. *AIP Conference Proceedings*[J], 2020, 23(3): 150002
- Stewart J, Williams D E. *Corrosion Science*[J], 1992, 33(3): 457
- Kityk A, Protsenko V, Pavlik V et al. *Chemistry and Chemical Technology*[J], 2019, 3: 1231
- Trent M C, Goods S H, Bradshaw R W. *AIP Conference Proceedings*[J], 2016, 1734(1): 160017
- Fernández A G, Lasanta M I, Pérez F J. *Oxidation of Metals*[J], 2012, 78: 329
- Sewell P B, Cohen M. *Journal of the Electrochemical Society*[J], 1964, 111(5): 501
- Stanislawski M, Wessel E, Hilpert K et al. *Journal of the Electrochemical Society*[J], 2007, 154: A295

Cu、Mo元素合金化对347H不锈钢组织与耐熔盐腐蚀性能影响

于志琦¹, 赵燕春¹, 刘天增^{1,2}, 冯力¹, 马虎文¹, 李具仓², 潘吉祥²

(1. 兰州理工大学 材料科学与工程学院 省部共建有色金属先进加工与再利用国家重点实验室, 甘肃 兰州 730050)

(2. 甘肃酒钢集团宏兴钢铁股份有限公司, 甘肃 嘉峪关 735100)

摘要: 对Cu、Mo元素合金化的347H不锈钢在565 °C的硝酸盐(60% NaNO₃+40% KNO₃)中进行长达720 h的静态腐蚀实验, 通过分析腐蚀产物的物相组成、微观形貌和化学成分, 研究Cu、Mo元素对347H不锈钢耐熔盐腐蚀的影响。结果表明: Mo元素可以细化晶粒, 使不锈钢具有耐腐蚀性能最好的中等晶粒度; 不锈钢在硝酸盐中发生均匀腐蚀, 腐蚀层为双层结构, 内外层均存在保护基体的腐蚀产物, 外层由Fe的氧化物层(Fe₂O₃、Fe₃O₄)、NaFeO₂层以及少量的MgFe₂O₄组成, 内层主要由尖晶石层(FeCr₂O₄、MgCr₂O₄)和Cu₂O薄层组成。Cu在内层被氧化形成致密的Cu₂O, 能有效阻隔O²⁻等离子向基体渗透。

关键词: 合金化; 347H不锈钢; 硝酸盐; 熔盐腐蚀

作者简介: 于志琦, 男, 2000年生, 博士生, 兰州理工大学省部共建有色金属先进加工与再利用国家重点实验室, 甘肃 兰州 730050, E-mail: 1020709191@qq.com